Ultramicroscopy 215 (2020) 113009

Contents lists available at ScienceDirect

Ultramicroscopy

journal homepage: www.elsevier.com/locate/ultramic

A general and robust analytical method for interface normal determination in TEM

Rui-Xun Xie[a], Melvyn Larranaga[b], Frédéric Mompiou[b], Nicolas Combe[b], Wen-Zheng Zhang[a,*]

[a] *Key Laboratory of Advanced Materials (MOE), School of Materials Science and Engineering, Tsinghua University, Beijing 100084, PR China*
[b] *CEMES-CNRS, Université de Toulouse, 29 rue J. Marvig, Toulouse 31055, France*

ARTICLE INFO

Keywords:
Transmission electron microscopy (TEM)
Trace analysis
Interface
Crystallography

ABSTRACT

This paper presents a new analytical method to determine interface normals from a series of bright/dark field images taken from arbitrary orientations. This approach, based on a general geometrical model of interface projection, provides a generalized formulation of existing methods. It can treat an excessive number of inputs, i.e. orientation conditions. Given 6 or more sets of inputs, even with considerable experimental errors, we prove that this method is still very likely to yield results with satisfactory accuracy. The robustness of the method can thus allow its implementation in problems dealing with a large amount of data. We show that this method can also be applied to determine 1D features or to check the planarity of microstructural features.

1. Introduction

Transmission electron microscopy (TEM) is a powerful tool to examine a variety of defects in materials, including point defects (zero dimension, 0D), dislocation lines (1D), interfaces (2D) and inclusions (3D). Since TEM images are 2D projections of the 3D space, the geometrical features of non-0D defects, e.g., their shapes, must be reconstructed from their projections on the observation plane. The identification of 3D inclusions, curved lines or curved planes is a cumbersome work [1,2]. However, many 1D or 2D defects, e.g., interfacial dislocations or faceted interfaces, often have preferred orientations. They can be considered as straight lines or flat planes. Accurately determining their crystallographic orientations is fundamental to unravel the mechanism of associated microstructure evolution [3]. In this context, the problem is restricted to the line direction or the interface plane normal determination, using a technique called trace analysis [4,5].

The concept and methods of trace analysis using TEM were clearly introduced in the well-known book by Hirsch et al. [4]. A line feature is always on the plane defined by its projection and the electron beam direction. Therefore it can be determined if observed from two directions. However, the projection of a planar feature usually contains the projection of two traces, the intersections of the interface with two foil surfaces, separated by a certain width. An interface can be directly determined at its edge-on condition, where the projection width is zero and the interface normal lies in the viewing screen [4]. Since an edge-on condition often carries non-negligible uncertainty, several modifications were later proposed to improve the accuracy, such as the single edge-on method [5,6], the double edge-on method [7,8], and the trace & edge-on method [9]. Despite their good accuracy, these methods are not easy to use, as finding an exact edge-on condition is usually time consuming or even impossible if it is out of the tilting range of the sample holder.

An edge-on condition is not always necessary, if the interface contains an additional sharp line feature, such as a straight dislocation line [6,10,11] or an intersection with another plane [12], using the so-called double-trace method. The orientations of both trace and the line feature in the plane can be measured by the trace analysis method of 1D features. Then one can obtain the interface normal by making a cross product of the line and the trace direction. However, additional line features are not always present, which limits the application of this method.

When the condition for the double-trace method is not satisfied, the projection width can be used to calculate interface normals at arbitrary orientations. In this approach, the trace direction is assumed to lie on the screen plane at zero tilt. The interface normal can be determined, once the inclination angle between the foil surface and the interface is determined. Traditionally, this was done by measuring the foil thickness and the projection width of the interface at an orientation near to zero tilt [5]. Since this method contains considerable uncertainty, Zhang et al. [13] made an improvement by tilting the sample along the trace direction. But it is usually difficult to ensure the tilting axis exactly

---

[*] Corresponding author.
E-mail address: zhangwz@tsinghua.edu.cn (W.-Z. Zhang).

https://doi.org/10.1016/j.ultramic.2020.113009
Received 17 February 2020; Received in revised form 14 April 2020; Accepted 25 April 2020

parallel with the trace direction. Qiu and Zhang [14] solved this problem on a single tilt holder by taking the angle between the trace and the tilting axis into consideration. In order to avoid ambiguous solutions, this approach still needs to track the trend of the projection width change during sample tilting. All these methods are based on the assumption that the upper and lower foil surfaces are both perpendicular to the electron beam direction at zero tilt. This may introduce systematic error when the foil has thickness variation or not flat.

Above methods are highly sensitive to experimental errors, since they rely on limited information — usually one or two sets of inputs (beam and projected trace directions, projection width). Particularly, the error could be greatly amplified by the cross product operation in double trace and double edge-on methods [9]. To improve the reliability, one may use excessive experimental data to calculate several solutions of the interface normal. The scattering of results can be plotted in a pole figure [9,14], but the selection of the final result and the estimation of its uncertainty are largely based on the operator's experience.

In order to improve the accuracy of interface normal determination and simplify the TEM operation, we present here a close-form algorithm to optimize the result with multiple sets of inputs from arbitrary orientations. In this method, there is no specific requirements on the beam direction, nor conditions on the interface and the foil.

In Section 2, we will describe the methodology used to compute the interface normal. Section 3 will present experimental details, followed by Section 4 illustrating the applications of the present method. The results and method will be further discussed in Section 5. The accuracy of the results will be addressed by an error analysis, and the method will be compared with other methods proposed in the literature. A generalization of our approach will be proposed at the end.

2. Geometrical model of interface projection

The approach presented below is a purely geometrical analysis of the orthogonal projection of planar features on the observation screen, without any requirement on the beam direction (projection direction) or the foil surface. It is based on the measurement of the interface width and apparent trace direction from different beam directions. The symbols used in the derivation and their definitions are listed in Table 1.[1]

A flat interface has two traces, the intersections with upper and lower foil surfaces. Firstly, let us assume the two foil surfaces to be parallel planes, resulting in two parallel traces separated by a certain width d. This case is shown in Fig. 1a, where the interface is enclosed by the red parallelogram $ABCD$. Line DC and AB are upper and lower traces of the interface. The blue parallelogram $EFGH$ is the projected interface on the screen. Areas of these parallelograms, $S_{ABCD} = d|AB|$ and $S_{EFGH} = w|EF|$, are related by $S_{EFGH} = S_{ABCD}\cos\psi$, where ψ is the angle between reversed electron beam direction $\boldsymbol{b}_\mathrm{e}$ and interface normal $\boldsymbol{n}$. Since $|EF|$ is the projection of $|AB|$, they are related by $|EF| = |AB|\cos\tau$, where τ is the angle between trace $\boldsymbol{t}$ and its projection $\boldsymbol{t}_\mathrm{p}$.

When the foil is bent or has a wedge shape, the assumption of parallel foil surfaces is no longer valid. Because of this, trace AB and trace DC are not parallel, and $ABCD$ in Fig. 1a is no longer a parallelogram (Fig. 1b). However, if a point on the interface can be tracked, it is still possible to resolve the relationship between d and w. As shown in Fig. 1b, by tracking point K on the interface $ABCD$, one can redefine d as the distance between K and the trace AB, while the distance between the projected point M and projected trace EF is measured as w[2]. Each time measuring w, the height of triangle EFM, it is crucial to make sure that point M at different tilts is the projection of the same point K. The area of interface triangle $S_{ABK} = d|AB|/2$ and that of projection triangle $S_{EFM} = w|EF|/2$ are still related by $S_{EFM} = S_{ABK}\cos\psi$. The relationship of $|EF| = |AB|\cos\tau$ remains valid.

Table 1
Definition of symbols.

Symbol	Definition
$\boldsymbol{b}_\mathrm{e}$	Reversed electron beam direction, unit vector
$\boldsymbol{n}$	Interface normal, unit vector
$\boldsymbol{s}$	Foil surface normal, unit vector
$\boldsymbol{t}$	Trace direction, i.e., direction of the intersection between the interface and the foil surface, unit vector $\boldsymbol{t} = \boldsymbol{n}\times\boldsymbol{s}/|\boldsymbol{n}\times\boldsymbol{s}|$
$\boldsymbol{t}_\mathrm{p}$	Projected direction of $\boldsymbol{t}$
h	Foil thickness
η	Azimuth angle from $\boldsymbol{x}_\mathrm{S}$ axis of the screen to $\boldsymbol{t}_\mathrm{p}$
d	Real interface width, i.e., real distance between traces
w	Projected interface width, i.e., distance between projected traces
i	Input number, index, $1 \le i \le m$
m	Total number of inputs
sgn(i)	A function that gives a value of ± 1 respect to the sign of $\boldsymbol{n}\cdot\boldsymbol{b}_\mathrm{ei}$

Therefore, no matter whether two foil surfaces are parallel or not, the interface projection width w is always given by

$$w = \frac{d\cos\psi}{\cos\tau} \tag{1}$$

Or alternatively using dot product:

$$w = \frac{|d\boldsymbol{n}\cdot\boldsymbol{b}_\mathrm{e}|}{\sqrt{1-(\boldsymbol{b}_\mathrm{e}\cdot\boldsymbol{t})^2}} \tag{2}$$

In Eq. (2), w and $\boldsymbol{b}_\mathrm{e}$ can be measured, while $d\boldsymbol{n}$ and $\boldsymbol{t}$ are unknown.

Vector $\boldsymbol{t}$ can be determined from its measured projections $\boldsymbol{t}_\mathrm{p}$'s at different $\boldsymbol{b}_\mathrm{e}$'s, using:

$$[\boldsymbol{b}_\mathrm{e1}\times\boldsymbol{t}_\mathrm{p1} \quad \boldsymbol{b}_\mathrm{e2}\times\boldsymbol{t}_\mathrm{p2} \quad \dots \quad \boldsymbol{b}_\mathrm{em}\times\boldsymbol{t}_{\mathrm{p}m}]^\mathrm{T}\boldsymbol{t} = \boldsymbol{0} \tag{3}$$

When Eq. (3) is solved by using the cross product $\boldsymbol{t} = (\boldsymbol{b}_{e1}\times\boldsymbol{t}_{p1})\times(\boldsymbol{b}_{e2}\times\boldsymbol{t}_{p2})$. When the number of input sets $m \ge 3$, it is an overdetermined homogeneous linear equation, and can be solved by the least square method (LSM, see Appendix A).

The determination of $\boldsymbol{t}$ allows to compute the non-linear part $\sqrt{1-(\boldsymbol{b}_\mathrm{e}\cdot\boldsymbol{t})^2}$ in Eq. (2), turning Eq. (2) into a linear problem. However, the width of interface projection, w_i, is always positive, while $\boldsymbol{n}\cdot\boldsymbol{b}_\mathrm{ei}$ could be negative. Thus sgn(i), the sign of $\boldsymbol{n}\cdot\boldsymbol{b}_\mathrm{ei}$, is needed to remove the absolute sign in Eq. (2). Using the fact that $d\boldsymbol{n}\cdot\boldsymbol{t} = 0$, a synthetic formula incorporating the input measurements (w_i, $\boldsymbol{b}_\mathrm{ei}$) can be derived:

$$\begin{bmatrix}\boldsymbol{b}_\mathrm{e1}^\mathrm{T}\\ \boldsymbol{b}_\mathrm{e2}^\mathrm{T}\\ \dots\\ \boldsymbol{b}_\mathrm{em}^\mathrm{T}\\ \boldsymbol{t}^\mathrm{T}\end{bmatrix}(d\boldsymbol{n}) = \begin{bmatrix}\mathrm{sgn}(1)w_1\sqrt{1-(\boldsymbol{b}_\mathrm{e1}\cdot\boldsymbol{t})^2}\\ \mathrm{sgn}(2)w_2\sqrt{1-(\boldsymbol{b}_\mathrm{e2}\cdot\boldsymbol{t})^2}\\ \dots\\ \mathrm{sgn}(m)w_m\sqrt{1-(\boldsymbol{b}_\mathrm{em}\cdot\boldsymbol{t})^2}\\ 0\end{bmatrix} \tag{4}$$

This equation can be solved by LSM, but the uncertainty of sgn(i) would result in multiple solutions of $d\boldsymbol{n}$. When $m = 2$, Eq. (4) is determined and two different solutions are expected. It is impossible to assess the actual one without additional information. When $m \ge 3$, Eq. (4) is overdetermined, and its residual error can be computed (see Appendix A). The uncertainty of sgn(i) will give 2^{m-1} solutions of $\boldsymbol{n}$. The one with the minimum residual error is the best solution, because an improper sgn(i) would result in significantly large residual error. The contribution to the residual error from each set of input (w_i, $\boldsymbol{b}_\mathrm{ei}$, $\boldsymbol{t}_\mathrm{pi}$) can be quantified by the respective element in the residual vector of Eq. (4) (see Appendix A). The element with the maximum absolute value and different sign from the others may indicate an abnormal input with significantly large deviation. One may drop this input and recalculate the result, which can reduce the residual error and improve the input

---

[1] If not pointed out, all the vector symbols noted in bold and italics are column vectors.

[2] Note that w is NOT the projection of d, as w is always perpendicular to EF, while the angle between EF and the projection of d will vary with the projection direction.

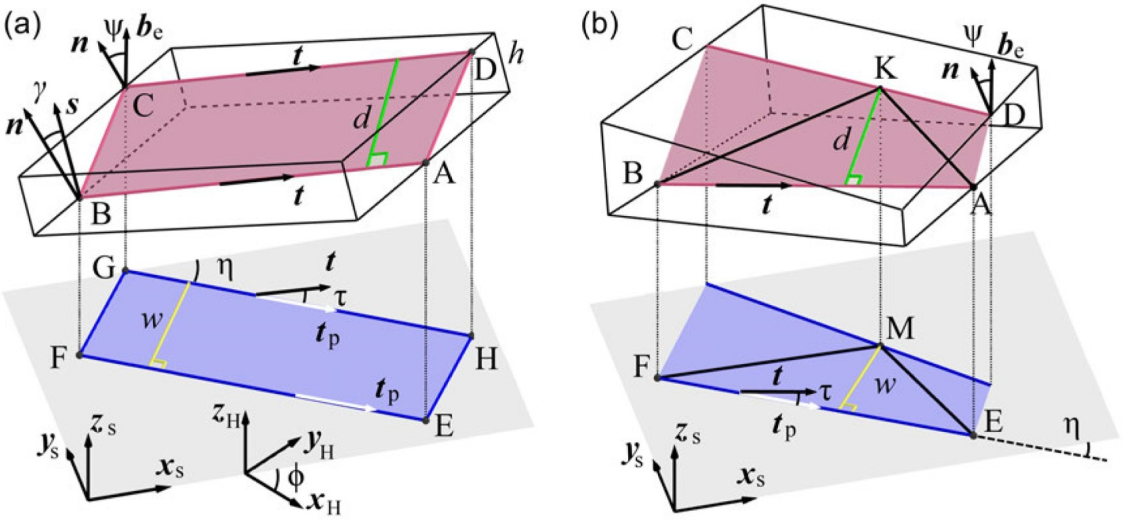

Fig. 1. Geometrical description of interface projection. (a) Parallel traces case: The interface *ABCD* is projected onto the viewing screen, giving the projection *EFGH*. (b) Non-parallel traces case: A traceable point *K* on the interface and a trace *AB* are projected to the viewing screen, giving the projection *EFM*.

consistency. Thus, with at least 3 different sets of experimental data (w_i, $\boldsymbol{b}_{ei}$, $\boldsymbol{t}_{pi}$), LSM will give the optimized solutions of $\boldsymbol{t}$, d and $\boldsymbol{n}$.

The accuracy of the interface normal, which is the deviation between the determined value and the true value, is an important concern. Unfortunately, the true value of $d\boldsymbol{n}$ is usually unknown, and needs to be estimated based on the internal consistency of inputs. The estimation of the true value is a range with a certain confidence, i.e., a confidence interval, which can represent the accuracy of the result. In the present work, the 92% confidence interval of d and that of $\boldsymbol{n}$ are calculated by the bootstrap method (see Appendix B) with Eq. (4).

A C++ implementation of the present algorithm can be found in Supplementary Materials.

3. Experimental details

The present method was tested in two cases. In both cases, bright field images were recorded at different orientation conditions in an FEI Tecnai G2 20 TEM operated at 200 kV. Observations were performed using a double tilt sample holder with coordinate conventions as shown in Fig. 2: in the holder coordinate system, the x-axis is parallel to the holder axis, and the y-axis is perpendicular to the x-axis and the beam direction. In the following, the subscripts $_H$, $_S$, and $_F$ denote the indices in holder (CS$_H$), screen (CS$_S$), and foil (CS$_F$) coordinate system (CS), respectively. In CS$_H$, the sample is firstly tilted about the $-\boldsymbol{y}$ axis by angle β, and then tilted about the $-\boldsymbol{x}$ axis by angle α.

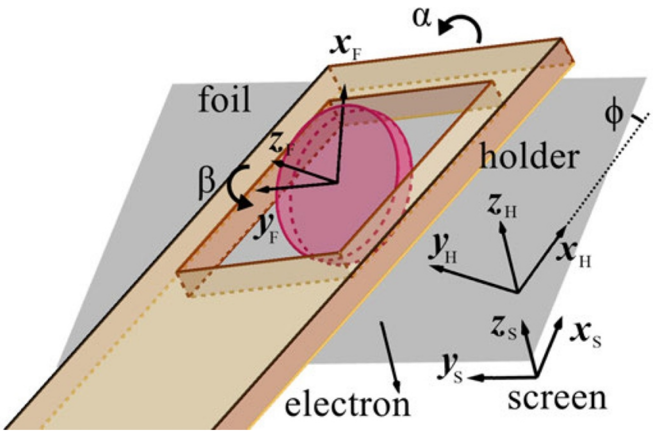

Fig. 2. Illustration of the holder coordinate system when the sample is mounted in a double-tilt holder.

The rotation angle from holder $\boldsymbol{x}_H$ axis to the projection screen $\boldsymbol{x}_S$ axis is ϕ about $\boldsymbol{z}_H = \boldsymbol{z}_S$ axis. This accounts for the rotation of the image in the microscope column. At zero tilt, CS$_F$ and CS$_H$ are identical. When the foil is tilted, CS$_F$ sticks to the foil, while CS$_H$ remains unchanged. Hence, the beam direction $\boldsymbol{b}_e$ perpendicular to the screen and the direction $\boldsymbol{t}_p$ in the observation plane can be calculated using right-handed rotation matrices Rx(θ), Ry(θ), and Rz(θ)(see Appendix D), as shown below:

$$\begin{aligned}\boldsymbol{b}_e &= [0,\ \ 0,\ \ 1]_S^T\\ &= [0,\ \ 0,\ \ 1]_H^T\\ &= \mathrm{Ry}(\beta)\mathrm{Rx}(\alpha)[0,\ \ 0,\ \ 1]_F^T\\ &= [\sin\beta\cos\alpha,\ \ -\sin\alpha,\ \ \cos\beta\cos\alpha]_F^T \qquad (5)\end{aligned}$$

$$\begin{aligned}\boldsymbol{t}_p &= [\cos\eta,\ \ \sin\eta,\ \ 0]_S^T\\ &= \mathrm{Rz}(\phi)[\cos\eta,\ \ \sin\eta,\ \ 0]_H^T\\ &= \mathrm{Ry}(\beta)\mathrm{Rx}(\alpha)\mathrm{Rz}(\phi)[\cos\eta,\ \ \sin\eta,\ \ 0]_F^T \qquad (6)\end{aligned}$$

where η is the azimuth angle between $\boldsymbol{t}_p$ and the $\boldsymbol{x}_S$ axis on the viewing screen.

In the first experiment, a grain with two interfaces was investigated in a duplex stainless steel Fe-24.9Cr-7.0Ni-3.1Mo (wt%) sample prepared by the same procedure as reported in [15]. The images were taken in conditions where $\phi = 90°$.

In the second case, a grain boundary with non-parallel traces was observed in an aluminum bicrystal with a misorientation close to a coincident $\Sigma 41\ 12.68^{\circ}\ <0\,0\,1>\ \{5\,4\,0\}$. The sample was first ground to a thickness of 50 microns using SiC grain disks and then electropolished to obtain electron transparency. The TEM foil was strained in-situ at about 400 °C, as reported earlier in [16]. Plastic deformation leads to a complex configuration of dislocations, resulting in significant bending of the wedge foil and possible deviation from the original orientation. Eq. (5) and Eq. (6) are still valid in this case, using here $\phi = 157°$ for Eq. (6).

4. Application examples

4.1. Measuring two interfaces with a double-tilt holder

Fig. 3 shows a series of bright field (BF) images of a faceted austenite grain (A) in a ferrite matrix (F) taken at different orientations. Two

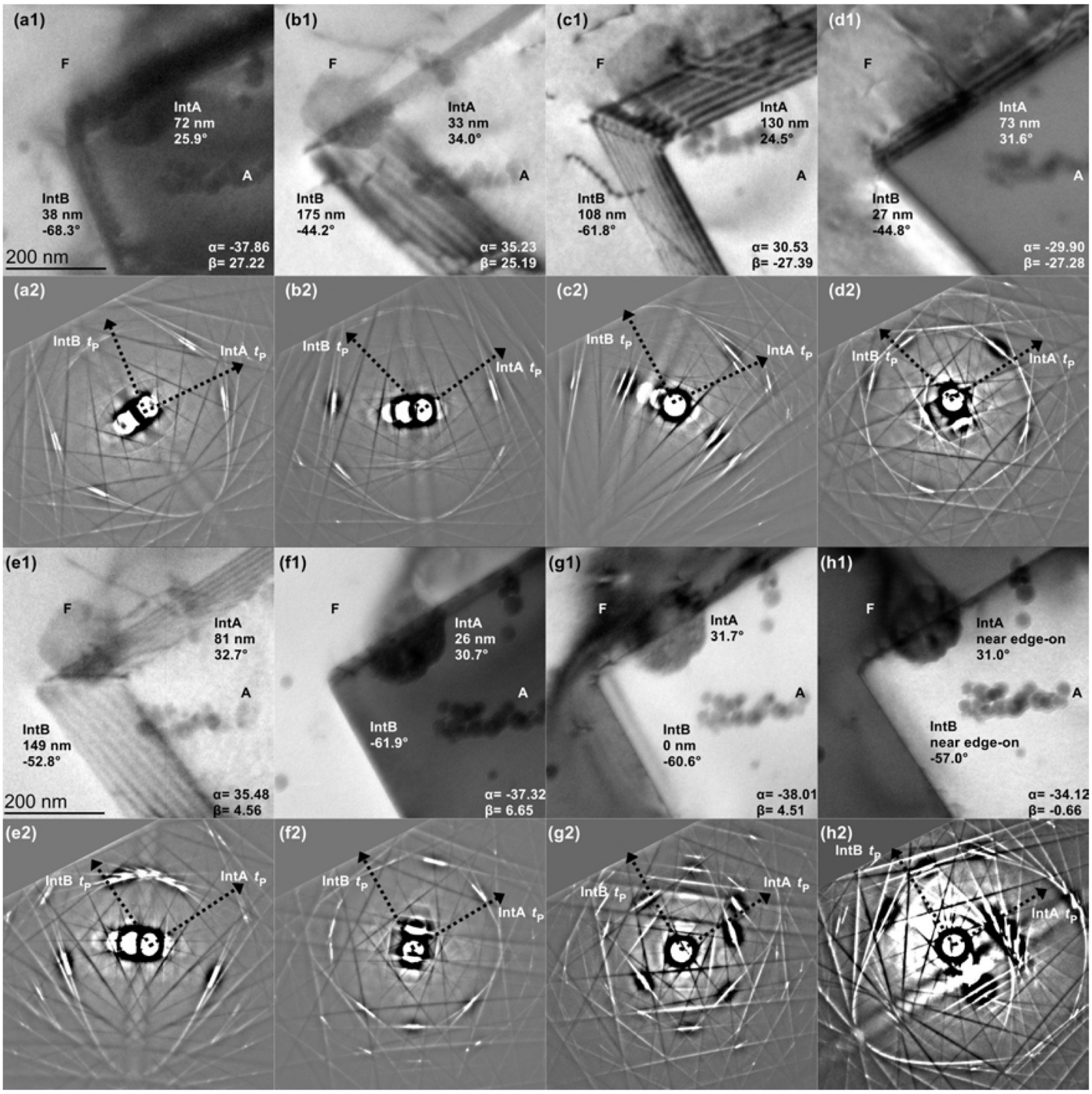

Fig. 3. BF images of the interfaces and the corresponding Kikuchi patterns taken in austenite at different tilt angles. The α and β tilt angles are reported in the bottom right. The projection widths and the azimuthal angle of both IntA and IntB interfaces are also indicated. Arrows in the Kikuchi patterns indicate the $\boldsymbol{t}_\mathrm{p}$ directions of IntA and IntB.

FCC/BCC facets, IntA and IntB, intersect and form a well defined corner. In order to show the ability to determine multiple interfaces, normals of these two facets were determined synchronously, using 6 sets of inputs among 8 different imaging conditions. The determination was performed both in $\mathrm{CS_F}$ and in the lattice coordinate system ($\mathrm{CS_L}$). The former is more convenient to use, as it only needs tilt angles of the sample holder, while the latter, which requires the analysis of Kikuchi patterns, usually has better accuracy. The normal of IntA is determined by Fig. 3a $\sim$ f, and that of IntB by Fig. 3a $\sim$ e and g. Fig. 3h, a near edge-on condition of both IntA and IntB, was only used to check the results.

The first step of this method is to determine $\boldsymbol{t}$. In $\mathrm{CS_F}$, the $\boldsymbol{b}_\mathrm{e}$'s were calculated using Eq. (5) with data in Table 2 and Fig. 3, while the $\boldsymbol{t}_\mathrm{p}$'s of IntA and IntB were calculated using Eq. (6) with their azimuth angle with respect to the $\boldsymbol{x}$ axis of Fig. 3a $\sim$ g. In $\mathrm{CS_L}$, $\boldsymbol{b}_\mathrm{e}$'s and $\boldsymbol{t}_\mathrm{p}$'s were defined in austenite using the Kikuchi patterns shown in Fig. 3, as listed in Table 2. Hence $\boldsymbol{t}$ was determined by solving Eq. (3) in either coordinate system.

The second step is to substitute $\boldsymbol{b}_\mathrm{e}$'s, $\boldsymbol{t}$, and w_i's, into Eq. (4) to solve $d\boldsymbol{n}$. By enumerating all the possibilities of $\mathrm{sgn_A}(i)$, and $\mathrm{sgn_B}(i)$, $d\boldsymbol{n}$ and its residual error in both conventions are solved by LSM. Among them, the one with the minimum residual error was chosen as the final result, whose $\mathrm{sgn}(i)$ is shown in Table 2. Then, the optimized results were calculated, as shown in Table 3. The $\boldsymbol{n}$'s determined in $\mathrm{CS_F}$ were transformed to lattice coordinates using the transformation matrix determined from Fig. 3e2 (see Supplementary materials).

The $\boldsymbol{t}$'s of IntA and IntB in $\mathrm{CS_F}$ are almost in the xOy plane, indicating that the foil was almost perpendicular to the beam direction at zero tilt. For each interface, the real width (d) and the normal ($\boldsymbol{n}$) calculated from different coordinate systems show a good consistency. This means $\mathrm{CS_F}$ can be used instead of $\mathrm{CS_L}$ to simplify the process while reserving the accuracy. The determined orientation of $\boldsymbol{n}$ is verified by tilting both interfaces to a near edge-on condition (Fig. 3h), where the interface normal $\boldsymbol{n}$ can be determined by $\boldsymbol{b}_\mathrm{e} \times \boldsymbol{t}_\mathrm{p}$. Using the data of Fig. 3h in Table 2, the normal of IntA is $[0.562\ 0.592\ -0.579]$, and that of IntB is $[-0.594\ -0.237\ -0.766]$. These results deviate 0.38° and 1.78° from the results determined in $\mathrm{CS_F}$ and deviate 1.34° and 1.12° from those in $\mathrm{CS_L}$. All the deviations are inside the confidence interval of the $\boldsymbol{n}$'s determined in Table 3. Hence, the present method is able to accurately determine multiple interfaces, either in $\mathrm{CS_F}$ or $\mathrm{CS_L}$.

Table 2
Directions in lattice coordinates from the Kikuchi patterns in Fig. 3 and sgn(i) for solving Eq. (4).

Figure	$\boldsymbol{b}_e$	IntA $\boldsymbol{t}_p$ IntB $\boldsymbol{t}_p$	$sgn_A(i)$ $sgn_B(i)$	w_{Ai} w_{Bi}	α(°)	β(°)
3 a	[-0.811 0.485 0.327]	[0.546 0.427 0.721] [0.249 0.792 -0.558]	-1 +1	72 38	-37.86	27.22
3 b	[-0.629 0.147 -0.763]	[-0.250 0.891 0.378] [0.772 0.239 -0.590]	+1 +1	33 175	35.23	25.19
3 c	[-0.107 0.628 -0.771]	[0.186 0.774 0.605] [0.963 -0.128 -0.238]	+1 +1	130 108	30.53	-27.39
3 d	[-0.281 0.951 0.130]	[0.485 0.023 0.874] [0.691 0.295 -0.660]	+1 -1	73 27	-29.90	-27.28
3 e	[-0.465 0.341 -0.817]	[-0.048 0.912 0.408] [0.885 0.157 -0.438]	+1 +1	81 149	35.48	4.56
3 f	[-0.677 0.684 0.272]	[0.597 0.295 0.746] [0.457 0.680 -0.574]	-1 not used	26 -	-37.32	6.65
3 g	[-0.654 0.704 0.277]	[0.612 0.277 0.741] [0.469 0.665 -0.582]	not used +1	- 0	-38.01	4.51
3 h	[-0.592 0.776 0.219]	[0.578 0.220 0.786] [0.541 0.584 -0.601]	not used not used	- -	-34.12	-0.66

Table 3
Results of trace directions and interface normals.

Coordinates	Interface	$\boldsymbol{t}$	$\boldsymbol{n}$	Confidence interval of $\boldsymbol{n}$ (°)	d (nm)
foil	IntA	$[0.453,\ -0.891,\ 0.003]_F$	$[-0.863,\ -0.432,\ 0.262]_F$ $[0.567\ 0.588\ -0.577]$	1.0	166 ± 5
	IntB	$[0.776, 0.630, 0.037]_F$	$[0.549,\ -0.670,\ 0.500]_F$ $[-0.605\ -0.208\ -0.769]$	1.8	178 ± 6
lattice	IntA	$[-0.215\ -0.581\ -0.785]$	$[0.581\ 0.585\ -0.567]$	1.6	172 ± 8
	IntB	$[-0.722\ -0.253\ 0.644]$	$[-0.610\ -0.240\ -0.755]$	1.6	182 ± 6

4.2. Measuring a grain boundary with non-parallel traces

Fig. 4 shows a series of BF images of an interface with non-parallel traces in an Al bicrystal sample taken at different tilt angles. The tracked point (pointed out by arrows) is defined by the position where the lower trace (dotted line) starts to deviate. Fig. 4a ~ e are used to solve the interface normal, while Fig. 4f is a near edge-on condition for verification. The trace $\boldsymbol{t}$ of the interface in CS_F deviates from the xOy plane, confirming that the foil is bent. Through a similar process as the previous example, the optimized result in CS_F is calculated as following: $\boldsymbol{t} = [0.883,\ -0.348,\ 0.315]_F$, $\boldsymbol{n} = [-0.473,\ -0.646,\ 0.600]_F$ with a 92% confidence interval of 2.4°, and $d = 224 \pm 12$nm. Using the transformation matrix determined from a Kikuchi pattern (Fig. S1), the lattice coordinates of the interface normal is $\boldsymbol{n} = [4.000\ -4.176\ 0.144]$ with 5.3° deviation from $[4\ -5\ 0]$. Noting that the 92% confidence interval is 2.4°, this deviation is considered to be the result of plastic deformation, rather than experimental errors. Using Eq. (5), the $\boldsymbol{b}_e$ at the near edge-on condition in Fig. 4f is $[0.278, 0.536, 0.797]_F$, which is almost perpendicular to the interface normal with 0.1° deviation. This edge-on condition confirms the result of $\boldsymbol{n}$. Therefore, the present method remains effective even for interfaces with non-parallel traces.

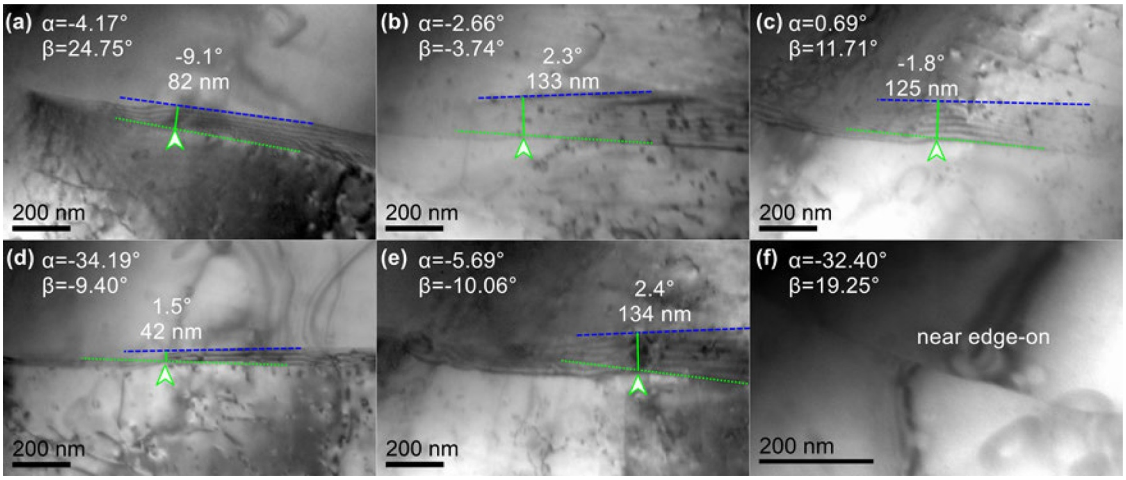

Fig. 4. BF images of the interface with non-parallel traces at different tilt angles. The α and β tilt angles are reported in the top left. The widths between the tracked point (indicated by arrows) and the trace (blue dashed line), and the azimuth angles of the trace (blue dashed line) are also indicated. (For interpretation of the references to colour in this figure legend, the reader is referred to the web version of this article.)

5. Discussion

5.1. Accuracy of $\boldsymbol{n}$

The use of the method presented here raises three questions concerning the accuracy of $\boldsymbol{n}$: (i) is the true value of the interface normal inside the bootstrap confidence interval; (ii) what is the main error source of interface normal determination; (iii) what is the optimal number of input datasets for an acceptable accuracy. To answer these questions, statistical analysis was performed using simulated erroneous data.

The simulated datasets were generated in $\mathrm{CS_F}$, using a 100-nm-thick virtual sample with two parallel surfaces normal to $\boldsymbol{z}$. As the prerequisite, the true value of the interface normal $\boldsymbol{n}$ must be known. Then, the α and β angles were randomly chosen in $\pm\ 40^\circ$ range, and the true values of w and η were calculated. The dataset (α, β, η, w) was randomly varied to simulate the experimental error. The α, β and η angles were randomly varied in $\pm\ 1^\circ$ range, while the projection widths in $\pm\ 5$ nm range. With several erroneous datasets, the interface normal was determined, and the deviation from the true value, which is called bias for clarity, was calculated.

In the first analysis, the interface normal was randomly chosen and determined with 6 sets of simulated data. This process was repeated for 10,000 times to calculate the coverage probability of the bootstrap confidence interval (how often it contains the true value). In our tests, the coverage probability ranges between 92.3% to 94.4%, which means the confidence level of the interval is at least 92%. The true value could be outside the confidence interval when the datasets (α, β, η, w) have relatively large systematic error, as this problem cannot be figured out from the consistency of the datasets.

In the second analysis, 4949 unit vectors evenly distributed on a hemisphere were used as known interface normals. For each normal, 6 arbitrary conditions (α, β, η, w) were used to compute back an erroneous normal, and its bias. Because the bias is dependent on the orientation conditions, it was averaged over 10,000 arbitrary condition sets for each known normal.

The results are plotted in a pole figure in Fig. 5a. It shows an *mm* symmetry due to the angular area covered by the sample tilt, limited by the dashed lines in Fig. 5a. The average bias of interface normals ranges between 0.65° and 1.35°, but most of the value is due to the error on w as shown in Fig. 5b, where the average bias is computed when varying only w. The ring-like shape of bias in Fig. 5a can be understood by inspecting how errors affect the value of $\cos\psi$ in Eq. (4). Using $h = d\sin\gamma = d\sqrt{1-(\boldsymbol{n}\cdot\boldsymbol{s})^2}$ (Fig. 1a) and Eq. (2), we can derive

$$\cos\psi = \boldsymbol{n}\cdot\boldsymbol{b}_\mathrm{e} = \frac{w}{h}\sqrt{1-(\boldsymbol{b}_\mathrm{e}\cdot\boldsymbol{t})^2}\,\sin\gamma \tag{7}$$

When the interface normal $\boldsymbol{n}$ moves from the center to the edge in the pole figure, $\sin\gamma = \sqrt{1-(\boldsymbol{n}\cdot\boldsymbol{s})^2}$ will increase, statistically making the value of $\cos\psi$ more sensitive to the error of w. In other words, largely inclined planes in the foil are less precisely determined, because they statistically present orientation conditions where the projection width is small. Meanwhile, the increase in ψ makes the direction of $\boldsymbol{n}$ less sensitive to the error of $\cos\psi$, as $\mathrm{d}\psi = -\mathrm{d}(\cos\psi)/\sin\psi$. The compromise of these two effects leads to a peak bias where the inclination angle between $\boldsymbol{n}$ and the foil normal is about 54° (Fig. 5b). In common cases, the projection of the interested interface is not very wide, which means that its normal is not inside the blue part in Fig. 5b. Therefore, the error of $\boldsymbol{n}$ mainly comes from the error of w.

In the third analysis, the interface normal was fixed to $[-0.547,\ 0.514,\ 0.661]_\mathrm{F}$, an orientation with the largest bias in Fig. 5a, while the number of input datasets varied from 3 to 15. The average of bias was computed, again by randomly varying the condition sets over 10,000 configurations. As shown in Fig. 5c, the average bias of $\boldsymbol{n}$ would reach 1.7° with 6 sets of inputs. It would reach 1.5° with 8 sets of inputs, but barely improves afterwards. Based on the above analysis, 6 to 8 sets of inputs would be the optimal choice.

In practice, it is not difficult to reach the data quality ($\pm\ 1^\circ$, $\pm\ 5$nm) in this analysis, and hence to get the results with the corresponding accuracy. Moreover, data quality can be further improved by image measurements at higher magnification, and by using Kikuchi patterns.

5.2. Comparison with existing methods

The geometry model used in the present method offers an inclusive framework to link existing methods. The double trace and edge-on methods can be considered as special cases of the present method in $\mathrm{CS_L}$, while existing projection width method used specific simplifications of the non-linear part $\sqrt{1-(\boldsymbol{b}_\mathrm{e}\cdot\boldsymbol{t})^2}$ in Eq. (2). The summary of the comparison is listed in Table 4.

In the double-trace method and edge-on methods, the interface normal is always derived by the cross product of two vectors. These two vectors can be two traces (double-trace), a projected trace and a beam direction (single edge-on), a trace and a beam direction (trace & edge-on), or two beam directions (double edge-on). Since the cross product is equivalent to LSM when solving a determined equation, these methods can all be treated as special cases of Eq. (4), with the traces determined by Eq. (3).

Existing projection width methods [13,14] treated the non-linear part $\sqrt{1-(\boldsymbol{b}_\mathrm{e}\cdot\boldsymbol{t})^2}$ in Eq. (2) with different strategies. Zhang et al. [13] tilted the sample about the trace direction, resulting in $\boldsymbol{b}_\mathrm{e}\cdot\boldsymbol{t}\equiv 0$ and $w = |d\boldsymbol{n}\cdot\boldsymbol{b}_\mathrm{e}|$. In their work, the sample thickness h was used rather than d. These two variables have a relationship, $h = d\cos\gamma$ (Fig. 1a), which is valid only if the two foil surfaces are both perpendicular to the beam direction at zero tilt. Qiu and Zhang [14] extended this work using the latter assumption, but they substituted $\sqrt{1-(\boldsymbol{b}_\mathrm{e}\cdot\boldsymbol{t})^2}$ by taking the tilting axis of the single-tilt sample holder, which happens to lie in the screen plane, as a reference vector. The derivation of this method using the

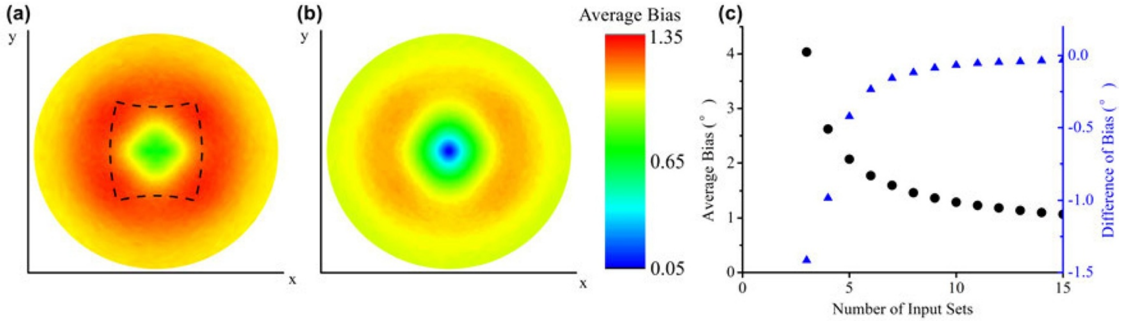

Fig. 5. Statistical analysis of the bias of the results. (a) Distribution of the average bias for interface normals chosen within the pole figure viewed from $\boldsymbol{z}$ axis. α, β, η and w have random errors. The beam directions reached by sample tilting are limited by dashed lines. (b) Same as (a) when the error is restricted to w. (c) The change of bias with respect to the number of inputs for a fixed interface normal.

Table 4
A comparison between this work and previous methods.

Method	Coordinates	Formulas	Special requirements	Number of inputs
double-trace [6]	lattice	Eq. (3)	another line feature	2
single edge-on [5]	lattice	Eq. (4)	edge-on condition	1
double edge-on [7]	lattice	Eq. (4)	edge-on condition	2
trace & edge-on [9]	lattice	Eq. (3) and Eq. (4)	edge-on condition	3
projection width [13]	holder	Eq. (4)	tilting about the trace	2
projection width [14]	holder	Eq. (C.4)	tilting axis in screen	2
this work	any	Eq. (3) and Eq. (4)	none	≥ 3

present geometry model is given in Appendix C.

The limitation of the reference vector method is that this vector $\boldsymbol{r}$ must be parallel to the tilting axis of the sample holder, otherwise the $\boldsymbol{n} \times \boldsymbol{s} \cdot \boldsymbol{r}$ in Eq. C.3 would not have a simple result like x, making it too hard to be solved. Therefore, this reference vector method is not applicable when the foil is tilted about more than one axis, because the resulted tilting axis is neither constant, nor in the screen plane.

In addition, the sign of w_i's remains a certain ambiguity and identification of the correct sign depends on the operator's experience in these two methods. As shown in this work, the use of at least 3 input sets enables the determination of the sign of w_i's straightforwardly.

5.3. Generalization of the present method

The plane determined by the present method is not necessary to be a real interface. It could be a virtual plane defined by 3 traceable points, e.g., points A, B, and K in Fig. 1b. This approach may thus be applied, for instance, to determine the dislocation habit plane[17], or to assess the planarity of 4 or more points.

The present method can also be used as an enhanced method to determine the length and the direction of 1D features. Let l be the projected length of the 1D feature and d be the original length of the 1D feature. Each measurement of a 1D feature projection ($\boldsymbol{b}_{\mathrm{ei}}, \boldsymbol{l}_{\mathrm{pi}}, l_i$) will give

$$[\boldsymbol{b}_{\mathrm{ei}} \times \boldsymbol{l}_{\mathrm{pi}} \quad \boldsymbol{b}_{\mathrm{ei}}]^{\mathrm{T}} d\boldsymbol{l} = [0 \quad l_i]^{\mathrm{T}} \tag{8}$$

Eq. (8) can be solved the same way as described above. The length vector of the 1D feature can thus be determined. This approach may be used to track accurately the distance between pining points on a dislocation line or the size of dislocation loops, as long as, 2 traceable features, such as intersection points between dislocation segments, can be detected.

Since all algorithms proposed here employed LSM, they are equally robust against random errors and scalable on large datasets. Efficient LSM functions can be found in plenty of math libraries, such as Eigen, LAPACK and Intel®MKL. Hence the present algorithms can be implemented as a real-time solver (as shown in Supplementary Material). They also have the potential to be integrated with automatic feature tracking in a tilting series, which could be a fast and efficient way to automatically measure microstructural features in a foil.

6. Conclusions

A new analytical method to determine interface normals with great capacity to intake excessive inputs has been proposed. It is a robust algorithm based on a generalized geometrical model of interface projection, and it can also automatically deal with a large amount of data. The effectiveness and accuracy of the method was verified using experimental observations of interfaces in TEM, regardless of the input orientation or foil surface configuration. Given 6 or a few more sets of inputs, even with considerable experimental errors, this method is still capable of yielding reliable results. The present method is compared with existing approaches, showing that many existing approaches can be treated as special cases of the present method, while the present method has fewer constraints. It can also be extended to determine 1D features or to check the planarity of a set of features.

Declaration of Competing Interest

The authors declare that they have no known competing financial interests or personal relationships that could have appeared to influence the work reported in this paper.

Acknowledgements

This work was supported by the National Natural Science Foundation of China [grant numbers: 51871131 and 51671111]; the National Key Research and Development Program of China [grant number 2016YFB0701304]; and the French National Research Agency (ANR) [grant number: RODIN ANR-17-CE08-0007].

Appendix A. LSM for solving overdetermined linear equations

For an overdetermined $\boldsymbol{Ax} = \boldsymbol{b}$ equation, e.g., Eq. (4) with $m \geq 3$, the least square solution of vector $\boldsymbol{x}$ is $\boldsymbol{x}^{+} = \boldsymbol{A}^{+}\boldsymbol{b}$, where $\boldsymbol{A}^{+}$ is Moore-Penrose inverse, or pseudo-inverse, of matrix $\boldsymbol{A}$. The solution has the residual vector, $\boldsymbol{e} = \boldsymbol{AA}^{+}\boldsymbol{b} - \boldsymbol{b}$, and the residual error, $|\boldsymbol{AA}^{+}\boldsymbol{b} - \boldsymbol{b}|$. This method is applicable for most circumstances. However, when $\boldsymbol{b} = \boldsymbol{0}$, e.g., Eq. (3), this method will only give a trivial solution of $\boldsymbol{x} = \boldsymbol{0}$. $\boldsymbol{Ax} = \boldsymbol{0}$ is a typical problem of overdetermined homogeneous linear system, whose solution is the eigen-vector of $\boldsymbol{A}^{\mathrm{T}}\boldsymbol{A}$ with the smallest eigen-value. The residual error of the solution is the smallest eigen-value.

Determination of sgn(i) in Eq. (4) needs to compare the residual error of the solution of each sgn(i) case. For example, let $d = 1$, $\boldsymbol{n} = [1\ 0\ 0]^{\mathrm{T}}$, $\boldsymbol{t} = [0\ 1\ 0]^{\mathrm{T}}$, and $\{\boldsymbol{b}_{\mathrm{ei}}^{\mathrm{T}}\} = \{1/2[\sqrt{2}\ 0\ \sqrt{2}],\ 1/2[-\sqrt{2}\ 0\ \sqrt{2}],\ 1/2[1\ 0\ \sqrt{3}]\}$. Then the theoretical values of $\{w_{\mathrm{i}}\}$ are $\{\sqrt{2}/2, -\sqrt{2}/2, 1/2\}$, while the measured ones are their absolute values $\{\sqrt{2}/2,\ \sqrt{2}/2,\ 1/2\}$. There are 4 possibilities of sgn(i): (+ + +), (+ + -), (+ - +), and (+ - -), and the residual errors of the solution based on them are 0.26, 0.97, 0, and 0.71, respectively. The one with the minimum residual error, (+ - +), is the proper sgn(i), which agrees with the theoretical value. In practice, this procedure should be done by computer programs, as demonstrated in Supplementary Materials.

Appendix B. Bootstrap method for estimating confidence intervals

Bootstrap is a statistical technique to estimate the variation of statistics that are computed from a set of data [18]. Here we use the bootstrap method to estimate the variation, i.e., confidence intervals, of d and $\boldsymbol{n}$ determined by Eq. (4). In Eq. (4), $\boldsymbol{t}$ and sgn(i) are considered as constant parameters in the equation, as they have already been determined. Thus, the data is composed of m data points of ($\boldsymbol{b}_{ei}$, w_i). Then, the data is resampled with replacement to generate a resampled data set of size m, with which the statistics d^* and $\boldsymbol{n}^*$ (star denoting resampled data) can be calculated. This procedure is repeated 10,000 times, the deviations between d^* and d and the angle between $\boldsymbol{n}^*$ and $\boldsymbol{n}$ can also be calculated. The confidence interval of d is given by the 95th percentile of the deviation of d^*. The confidence interval of $\boldsymbol{n}$ is given by the 95th percentile of the deviation angle of $\boldsymbol{n}^*$, denoting a confidence cone around $\boldsymbol{n}$ [19]. Usually using the 95th percentile will result in a confidence level of 95%. However, $\boldsymbol{t}$ in Eq. (4) also contains some error, which may degrade the internal consistency and thus the confidence level. As tested in Section 5.1, the confidence level is greater than 92%.

Appendix C. The projection width method reported in [14]

Here we used the symbols and equations in present work to derive the equations reported in [14].

By replacing $\boldsymbol{t}$ in Eq. (2) with $\boldsymbol{n} \times \boldsymbol{s}/|\boldsymbol{n} \times \boldsymbol{s}|$, and temporarily ignoring the absolute sign on $\boldsymbol{b}_\mathrm{e} \cdot \boldsymbol{n}$, we get:

$$w = \frac{h\boldsymbol{b}_\mathrm{e}\cdot\boldsymbol{n}}{\sqrt{1-(\boldsymbol{n}\cdot\boldsymbol{s})^2-(\boldsymbol{n}\times\boldsymbol{s}\cdot\boldsymbol{b}_\mathrm{e})^2}} \tag{C.1}$$

By introducing $\boldsymbol{r}$, the angle η between $\boldsymbol{t}_\mathrm{p}$ and $\boldsymbol{r}$ is expressed by:

$$\cos\eta = \frac{\boldsymbol{t}_\mathrm{p}\cdot\boldsymbol{r}}{|\boldsymbol{t}_\mathrm{p}|} = \frac{\boldsymbol{n}\times\boldsymbol{s}\cdot\boldsymbol{r}}{\sqrt{1-(\boldsymbol{n}\cdot\boldsymbol{s})^2-(\boldsymbol{n}\times\boldsymbol{s}\cdot\boldsymbol{b}_\mathrm{e})^2}} \tag{C.2}$$

By substituting Eq. (C.2) into Eq. (C.1), we get Eq. (C.3). h and $\boldsymbol{n}$ have to be combined, for they both need solving.

$$\boldsymbol{b}_\mathrm{e}\cdot\left(\frac{h}{\boldsymbol{n}\times\boldsymbol{s}\cdot\boldsymbol{r}}\boldsymbol{n}\right) = \frac{w}{\cos\eta} \tag{C.3}$$

In the work of Qiu and Zhang, the sample is tilted about $\boldsymbol{y}$ axis with the screen remains unchanged. The $\boldsymbol{x}^\mathrm{r}$, $\boldsymbol{y}^\mathrm{r}$, $\boldsymbol{z}^\mathrm{r}$ vectors at zero tilt in their work are the basis vectors in the holder coordinates system. Therefore, the parameters should be set as $\boldsymbol{b}_\mathrm{e} = [0,\ 0,\ 1]_\mathrm{H}^\mathrm{T}$, $\boldsymbol{r} = [0,\ -1,\ 0]_\mathrm{H}^\mathrm{T}$, $\boldsymbol{n} = \mathrm{Ry}(\alpha)[x,\ y,\ z]_\mathrm{H}^\mathrm{T}$, and $\boldsymbol{s} = \mathrm{Ry}(\alpha)[0,\ 0,\ 1]_\mathrm{H}^\mathrm{T}$. In addition, the trace direction was measured at zero tilt angle by η_0, which would directly give $\boldsymbol{t}$. Similar as Eq. (4), Eq. (C.4) is constructed using two sets of Eq. (C.3) and $\boldsymbol{t}\cdot\boldsymbol{n} = 0$. The ± sign is caused by the uncertainty of w_i signs, and should be eliminated by inspecting the trend of projection width change.

$$\begin{bmatrix} -\sin\alpha_1 & 0 & \cos\alpha_1 \\ -\sin\alpha_2 & 0 & \cos\alpha_2 \\ \sin\eta_0 & -\cos\eta_0 & 0 \end{bmatrix} \frac{h}{x} \begin{bmatrix} x \\ y \\ z \end{bmatrix} = \begin{bmatrix} w_1/\cos\eta_1 \\ \pm\, w_2/\cos\eta_2 \\ 0 \end{bmatrix} \tag{C.4}$$

The solution of Eq. (C.4) is Eq. (C.5), the same as reported in their work.

$$\begin{bmatrix} h \\ hy/x \\ hz/x \end{bmatrix} = \frac{1}{\sin(\alpha_2-\alpha_1)} \begin{bmatrix} \dfrac{w_1\cos\alpha_2}{\cos\eta_1} \mp \dfrac{w_2\cos\alpha_1}{\cos\eta_2} \\ \left(\dfrac{w_1\cos\alpha_2}{\cos\eta_1} \mp \dfrac{w_2\cos\alpha_1}{\cos\eta_2}\right)\tan\eta_0 \\ \dfrac{w_1\sin\alpha_2}{\cos\eta_1} \mp \dfrac{w_2\sin\alpha_1}{\cos\eta_2} \end{bmatrix} \tag{C.5}$$

Appendix D. Rotation matrices

Matrices Rx(θ), Ry(θ), Rz(θ) are right-handed rotation matrices with rotation angle θ about x, y, z axis respectively.

$$\mathrm{Rx}(\theta) = \begin{bmatrix} 1 & 0 & 0 \\ 0 & \cos\theta & -\sin\theta \\ 0 & \sin\theta & \cos\theta \end{bmatrix} \tag{D.1}$$

$$\mathrm{Ry}(\theta) = \begin{bmatrix} \cos\theta & 0 & \sin\theta \\ 0 & 1 & 0 \\ -\sin\theta & 0 & \cos\theta \end{bmatrix} \tag{D.2}$$

$$\mathrm{Rz}(\theta) = \begin{bmatrix} \cos\theta & -\sin\theta & 0 \\ \sin\theta & \cos\theta & 0 \\ 0 & 0 & 1 \end{bmatrix} \tag{D.3}$$

Supplementary material

Supplementary material associated with this article can be found, in the online version, at 10.1016/j.ultramic.2020.113009

References

[1] P.A. Midgley, R.E. Dunin-Borkowski, Electron tomography and holography in materials science, Nat. Mater. 8 (2009) 271, https://doi.org/10.1038/nmat2406.

[2] J.S. Barnard, J. Sharp, J.R. Tong, P.A. Midgley, High-resolution three-dimensional imaging of dislocations, Science 313 (5785) (2006), https://doi.org/10.1126/science.1125783. 319–319

[3] W.-Z. Zhang, X.-F. Gu, F.-Z. Dai, Faceted interfaces: a key feature to quantitative understanding of transformation morphology, Npj Comput. Mater. 2 (2016) 16021, https://doi.org/10.1038/npjcompumats.2016.21.

[4] P. Hirsch, A. Howie, R.B. Nicholson, D. Pashley, M. Whelan, Electron microscopy of thin crystals, Butterworths, London, 1965.

[5] J.W. Edington, K.T. Russell, Practical electron microscopy in materials science, Macmillan International Higher Education, 1977.

[6] B. Sandvik, C. Wayman, Characteristics of lath martensite: part I. Crystallographic and substructural features, Metall. Trans. A 14A (1983) 809–822.

[7] C.P. Luo, X.L. Xiao, D.X. Wu, A TEM method for accurate measurement of habit plane (interface): double edge-on trace analysis, Prog. Nat. Sci. 7 (6) (1997) 742–748.

[8] D. Qiu, W.-Z. Zhang, A TEM study of the crystallography of austenite precipitates in a duplex stainless steel, Acta Mater. 55 (20) (2007) 6754–6764, https://doi.org/10.1016/j.actamat.2007.08.024.

[9] Y. Meng, L. Gu, W.-Z. Zhang, Precise determination of the irrational preferred interface orientation by TEM, Acta Metall. Sin. 46 (4) (2010) 411, https://doi.org/10.3724/SP.J.1037.2009.00577.

[10] C.T. Young, J.H. Steele, J.L. Lytton, Characterization of bicrystals using Kikuchi patterns, Metall. Trans. 4 (9) (1973) 2081–2089, https://doi.org/10.1007/bf02643271.

[11] Q. Liu, A new method for determining the normals to planar structures and their trace directions in transmission electron-microscopy, J. Appl. Crystallogr. 27 (1994) 762–766, https://doi.org/10.1107/S0021889894002621.

[12] S. Li, Y. Zhang, C. Esling, J. Muller, J.-S. Lecomte, G.W. Qin, X. Zhao, L. Zuo, Determination of surface crystallography of faceted nanoparticles using transmission electron microscopy imaging and diffraction modes, J. Appl. Crystallogr. 42 (3) (2009) 519–524, https://doi.org/10.1107/s0021889809013107.

[13] M.X. Zhang, P.M. Kelly, J.D. Gates, Determination of habit planes using trace widths in TEM, Mater. Charact. 43 (1) (1999) 11–20, https://doi.org/10.1016/S1044-5803(98)00053-9.

[14] D. Qiu, M.X. Zhang, A simple and inclusive method to determine the habit plane in transmission electron microscope based on accurate measurement of foil thickness, Mater. Charact. 94 (2014) 1–6, https://doi.org/10.1016/j.matchar.2014.04.008.

[15] J. Du, F. Mompiou, W.-Z. Zhang, In-situ TEM study of dislocation emission associated with austenite growth, Scr. Mater. 145 (2018) 62–66, https://doi.org/10.1016/j.scriptamat.2017.10.014.

[16] A. Rajabzadeh, M. Legros, N. Combe, F. Mompiou, D. Molodov, Evidence of grain boundary dislocation step motion associated to shear-coupled grain boundary migration, Philos. Mag. 93 (10–12) (2013) 1299–1316, https://doi.org/10.1080/14786435.2012.760760.

[17] S. Naanani, J.-P. Monchoux, C. Mabru, A. Couret, Pure climb of [001] dislocations in TiAl at 850°C, Scr. Mater. 149 (2018) 53–57.

[18] B. Efron, Computers and the theory of statistics: thinking the unthinkable, SIAM Rev. 21 (4) (1979) 460–480.

[19] N.I. Fisher, P. Hall, Bootstrap confidence regions for directional data, J. Am. Stat. Assoc. 84 (408) (1989) 996–1002, https://doi.org/10.2307/2290075.